Quantification of fcc-Ge2Sb2Te5 stoichiometry variations

Guillaume Roland, Alain Portavoce, Maxime Bertoglio, Marion Descoins, Jacopo Remondina, Frédéric Lorut, Magali Putero

MTLA 32 (2023) 101885

Contents lists available at ScienceDirect

Materialia

journal homepage: www.elsevier.com/locate/mtla

Full Length Article

Quantification of fcc-$Ge_2Sb_2Te_5$ stoichiometry variations

Guillaume Roland [a,b], Alain Portavoce [a,*], Maxime Bertoglio [a], Marion Descoins [a], Jacopo Remondina [a], Frédéric Lorut [b], Magali Putero [a]

[a] CNRS, IM2NP UMR7334, Campus Scientifique de St Jérôme, Aix-Marseille University, 13397 Marseille cedex 20, France
[b] STMicroelectronics, 850 rue Jean Monnet, Crolles 38920, France

ARTICLE INFO

Keywords:
$Ge_2Sb_2Te_5$
Phase change material
Phase change random access memory

ABSTRACT

Ge-rich Ge-Sb-Te (GGST) alloys are being currently integrated to the complementary metal oxide semiconductor technology for industrial production of new generation of non-volatile memories, able to support the development of raising technologies such as internet-of-things and artificial intelligence. These phase-change random access memories are based on ultra-fast reversible crystallization/amorphization of the $Ge_2Sb_2T_5$ (GST225) chalcogenide compound exhibiting a large resistivity contrast between the amorphous and crystalline states. GGST film crystallization is accompanied by the phase separation of Ge and an fcc-GST225 phase of unknown composition, which should vary with Ge excess of GGST films. However, device properties and reliability are expected to vary with fcc-GST225 stoichiometry. This work reports atom probe tomography, X-ray diffraction, and scanning transmission electron microscopy investigations of the crystallization of an amorphous GST225 layer containing pseudo-periodic local composition variations. The results show that the compound fcc-GST225 is not stoichiometric, accepting 10 Ge at% variations, 7.5 Sb at% variations, and 6 Te at% variations. Furthermore, the microstructure as well as element distributions in the crystallized fcc-GST225 film suggest that fcc-GST225 nucleation is piloted by local composition variations. Fcc-GST225 nuclei formed in the Te-richest regions of the amorphous layer, corresponding to bulk hetero-nucleation, lowering the nucleation temperature.

1. Introduction

Phase change materials (PCM) and phase change random access memories (PCRAM) are expected to support the development of next-generation technologies such as Internet-of-Things [1,2] and artificial intelligence technologies [3–7], with applications in a wide range of domains from automotive (autonomous vehicles) [8–11] to health [7, 12] and environmental [13,14] domains, for example. PCM-based technologies use the large difference of optical, electrical, or thermal properties between the material amorphous and crystalline states, as well as the nanosecond-speed reversible switch between these two states [15,16]. Among PCM, Ge-Sb-Te (GST) chalcogenide compounds are studied with great interest as such materials are compatible with the complementary metal oxide semiconductor (CMOS) technology, having a strong impact on technology as well as industrial production potentials. Indeed, the CMOS technology allows the production of highly reliable micro- to nano-devices at relatively low cost and high production rate, and offers strong integration potential [8,10,17]. In particular, GST-based technology involves much lower fabrication thermal budgets as well as a different integration scheme compared to Si(Ge) technology, allowing GST devices to be integrated on top of current microelectronic devices on the same Si wafer [8,10,17,18].

PCRAM combines fast programming (nanosecond Write-time), high scalability and higher endurance compared to usual non-volatile memories [19,20]. They are based on PCM, and can be used for neuro-inspire as well as all-photonic in-memory computing [3,7,21,22]. The prototypical GST compound $Ge_2Sb_2Te_5$ (GST225) has been largely studied as suitable candidate for PCRAM [2–5]. However, its relatively low crystallization temperature ($T_X \sim 150$°C [10]) is incompatible with some industrial techniques, such as the soldering reflow process, and high-temperature data retention required for automotive markets [10, 23–25].

Consequently, instead of GST layers with the “225” stoichiometry, Ge-rich GST (GGST) alloys with Ge composition higher than 30% are considered for industrial production, since T_X of GST225 was shown to increase linearly with GGST alloy Ge composition [10,26]. However, the alloy crystallization is characterized by the phase separation of Ge and GST225 starting in the amorphous state in this case, leading to the

* Corresponding author.
E-mail address: alain.portavoce@im2np.fr (A. Portavoce).

https://doi.org/10.1016/j.mtla.2023.101885
Received 15 June 2023; Accepted 31 August 2023
Available online 2 September 2023

formation of Ge and fcc-GST225 nano-grains [25,27,28]. The microstructure of crystallized GGST layers is generally characterized using X-ray diffraction (XRD) and transmission electron microscopy (TEM), including scanning TEM (STEM), Energy-dispersive X-ray spectroscopy (EDS) and Electron Energy Loss Spectroscopy (EELS) [25–33]. However, the composition of fcc-GST225 grains is difficult to quantitatively determine. EDS measurements [27] as well as ab initio calculations [34–36] reported so far in the literature suggest that the composition of fcc-GST225 grains crystallized from amorphous GGST layers does not match the "225" stoichiometry. Furthermore, recent atomistic kinetic Monte Carlo simulations showed that the experimental crystallization kinetics of GGST layers can be explained by a significant off-stoichiometry degree of the fcc-GST225 phase [26]. It is important to stress that any composition variation could influence the fcc-GST225 properties of interest [24,26,33,37–39], and thus could have an impact on device properties. If the compound fcc-GST225 accepts substantial composition variations, the stoichiometry of the fcc-GST225 nano-grains in GGST layers is probably different for different Ge excess. The knowledge of the fcc-GST225 phase stoichiometry is thus mandatory.

The goal of the present experiments is to answer two essential questions. First, is the phase fcc-GST225 stoichiometric? And if not, what is its composition degree of variation? And second, if fcc-GST225 not stoichiometric, what is the effect of local composition variations on GST225 crystallization? To this aim, the composition of a GST225 layer containing pseudo-periodic composition variations was quantitatively measured in three-dimensional space (3D) at the atomic scale by atom probe tomography (APT), and compared to the layer microstructure studied by XRD and STEM.

2. Methods

A 300 nm-thick amorphous GST225 (a-GST225) layer was deposited by magnetron sputtering on a substrate made of a 20 nm-thick TiN layer on Si(001). The TiN layer acts as a diffusion barrier between the deposited layer and the Si atoms of the substrate. A-GST225 deposition was performed at room temperature (RT) in a commercial magnetron sputtering system exhibiting a base pressure of 10^{-8} mbar. Sputtering was achieved using a 99.9999% pure Ar gas flow under a work pressure of 3.6×10^{-3} mbar. Ge, Sb, and Te were co-sputtered from three monoatomic targets exhibiting a purity of 99.999%, 99.99%, and 99.99%, respectively. Ge and Sb were sputtered in the DC mode, while Te was sputtered in the RF mode. Ge, Sb and Te fluxes were calibrated separately by measuring the thickness of sputtered films deposited at RT on the native oxide of Si(001) substrates by X-ray reflectivity. The sample was rotating at the speed of 5 rpm during deposition, and the 300 nm-thick GST225 layer was capped with 10 nm of pure Ge at the same temperature in order to minimize oxidation effect. After deposition, the sample was annealed under a vacuum of $\sim 10^{-4}$ mbar *in situ* in the XRD setup, following a heating ramp of ~ 0.9°C min^{-1} between 100°C and 250°C. These annealing conditions usually allow GST225 full crystallization and allow the crystallization temperature T_X to be determined as the temperature at which the phase is first detected in the DRX pattern [26]. $T_X = 140$°C in the present case. The sample crystallization was investigated by both XRD in the Bragg-Brentano geometry (θ–2θ) using a Panalytical Empyrean diffractometer equipped with an PIXcel detector and a Cu K-α source ($\lambda = 0.154$ nm), and by STEM using a Tecnai OSIRIS TEM from FEI operating at 200 kV. TEM lamellas were prepared using the in-situ lift out technique in a FIB-SEM system Helios450^{TM} from ThermoFisher and mounted onto a copper grid. The final thinning of the lamella was performed using an acceleration voltage of 2 kV. The composition of the samples before and after annealing was measured by APT using a CAMECA LEAP 3000X-HR system in laser mode at $T = 50$ K, with a laser energy of 0.5 nJ, a laser pulse frequency of 100 kHz, and an evaporation rate of 0.1%. The APT samples were prepared by focus ion beam (FIB) using a Helios NanoLab DualBeam Ga^+ FIB from FEI, following the procedure described in [40]. The size of APT reconstructed volumes was set to match TEM and EDS observations. Fig. 1 presents a typical mass spectrum obtained by APT (no difference between amorphous and crystalline films) with mass-to-charge-state peak identification. Few peaks were not identified (uncolored in Fig. 1). However, they correspond to less than 1% of all the atoms. Furthermore, among them, less than 0.4% could be suspected to contribute to the GST alloy composition. Fig. 1 shows also the details of mass-to-charge-state peak identification in the three regions of the mass spectrum where molecules are overlapping.

3. Results and discussion

The GST225 layer (300 nm-thick) was deposited using magnetron co-sputtering of Ge, Sb and Te targets. The Ge, Sb, and Te deposition fluxes during deposition were set to match the stoichiometry of the compound GST225. However, due to the geometry of the sputtering system [41], the continuous rotation of the sample during co-deposition of the three elements leads to the formation of pseudo-periodical composition variations along the depth of the layer [41]. This deposition process allowed the deposition of amorphous GST225 layers (a-GST225) exhibiting an overall GST stoichiometry matching the "225" stoichiometry, but containing local concentration variations along the layer thickness. The substrate performed 15 rotations during deposition (181 seconds). Fig. 2 presents the X-ray diffractogram acquired on the as-deposited sample (black solid line, star symbol).

As expected, the film is amorphous due to room temperature (RT) deposition. Fig. 3 shows a 50 nm-deep volume of the a-GST225 layer analyzed by APT, as well as the Ge, Sb, and Te concentration profiles measured in this volume along the layer depth. The entire volume contains 29.0 at% of Ge, 22.1 at% of Sb, and 48.9 at% of Te that is close to the stoichiometry of the GST225 compound. Several volumes were analyzed giving similar results. The 7 Ge at% excess, corresponding to a 7 Te at% deficiency, can be due to co-sputtering flux interactions, inaccuracy in determining deposition rates [42], or the result of a lack of statistic due to the limited lateral size of the APT volumes.

Fig. 3b shows that the atomic distributions are not homogeneous along the depth of the a-GST layer, as expected [41]. The concentration profiles are not constant, and pseudo-periodic concentration variations exhibiting periods between 20 (Ge and Te) and 25 nm (Sb) are observed. One can note that the Ge and Te concentration profiles are in opposition of phase, while the Sb variation phase is in between. In average, the local concentration variations of the elements (C) in the layer are $17.5 \leq C_{Ge} \leq 35$ at%, $15 \leq C_{Sb} \leq 30$ at%, and $42.5 \leq C_{Te} \leq 62.5$ at%, corresponding to the average concentration differences $\Delta C_{Ge} \sim 17.5$ at%, $\Delta C_{Sb} \sim 15$ at %, and $\Delta C_{Te} \sim 20$ at%.

Fig. 4 presents APT analyses performed on the GST225 layer after thermal ramp annealing up to 250°C. According to XRD measurements (red solid line, diamond symbol in Fig. 2), this layer was crystallized during annealing, and fcc-GST225 is the only phase detected since the six diffraction peaks detected at $2\theta = 25.67°$, $29.66°$, $42.51°$, $50.26°$, $52.56°$, and $61.50°$ correspond to the atomic planes (111), (200), (220), (311), (222), and (400) of fcc-GST225. Fig. 4a shows a 195 nm-deep volume of the crystallized GST225 layer analyzed by APT. The top volume presents the entire atomic distribution, while the three others display Ge, Sb, and Te iso-concentration surfaces in the same volume. The overall composition of the analyzed volume is 24.7 at% of Ge, 21.5 at% of Sb, and 53.8 at% of Te. This stoichiometry is closer to the "225" stoichiometry compared to the overall stoichiometry found in the APT volumes analyzed in the as-deposited GST225 layer. The Ge excess and the Te deficiency are reduced to 2.7 at% and 2.2 at%, respectively. This result suggests that the composition difference between the expected composition (from sputtering flux calibration) and the APT measurements is mainly related to the reduced statistic in the APT volumes, which do not include long-range composition inhomogeneity (in particular in the direction parallel to the sample surface). Each iso-

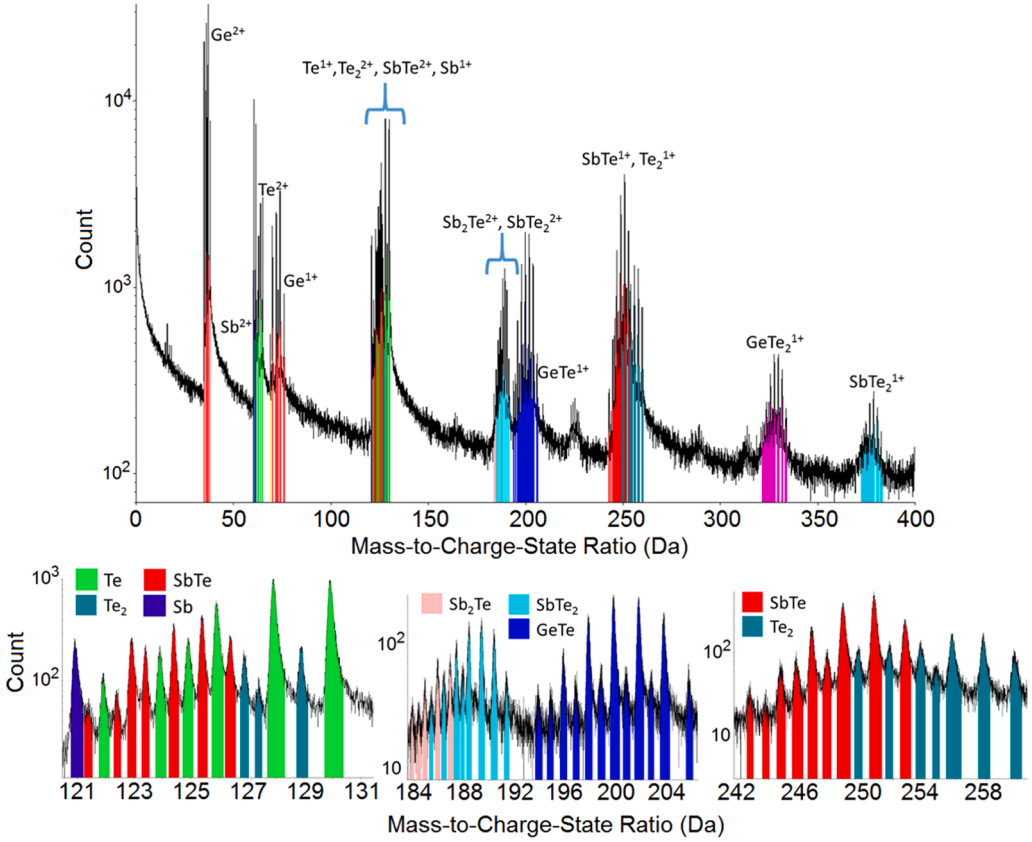

Fig. 1. Mass spectrum of an entire APT volume obtained from a crystallized GST225 film.

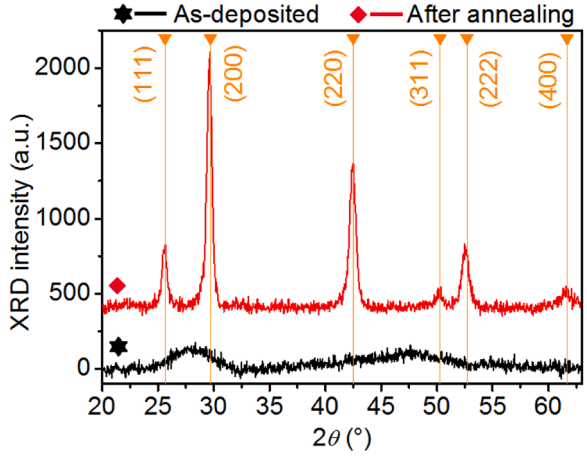

Fig. 2. XRD measurements performed on the sample before (black solid line, star symbol) and after (red solid line, diamond symbol) thermal ramp annealing up to 250°C.

surface of concentration C_{iso} in Fig. 4a delimits a volume in the sample in which the concentration of the considered element (Ge, Sb, or Te) is higher than C_{iso} ($C_{iso\text{-}Ge} = 27.6$ at%, $C_{iso\text{-}Sb} = 22.8$ at%, and $C_{iso\text{-}Te} = 55.3$ at% in Fig. 4a). These iso-concentration surfaces reveal the periodical distribution of the elements along the depth of the layer. Depending on the element, 10 (for Ge) to 11 (for Sb) regions exhibiting a high amount of one of the given elements are found to be regularly separated, from the top to the bottom of the volume analyzed by APT. The local pseudo-periodic composition variations initiated in the amorphous as-deposited film, due to the rotation of the substrate below the three sputtered monoatomic targets, led to the formation of local composition variations

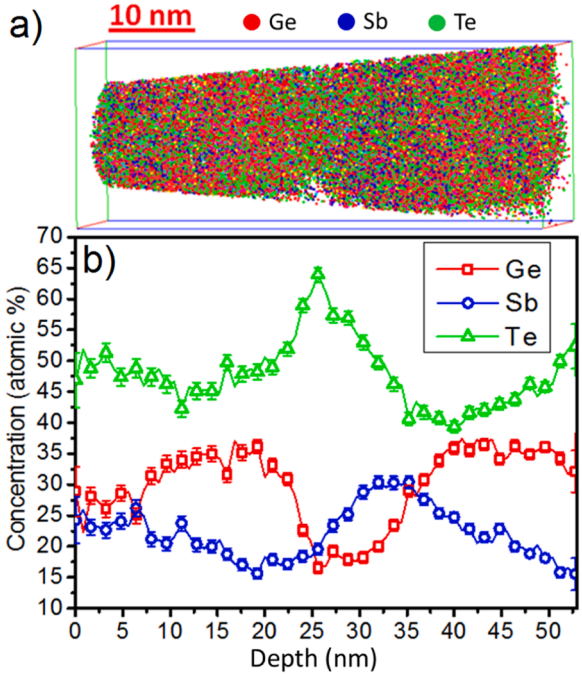

Fig. 3. APT measurements performed on the as-deposited sample: a) APT volume showing the entire atomic distribution, each point is a single atom (red for Ge, blue for Sb, and green for Te), and b) Ge (red squares), Sb (blue circles), and Te (green triangles) concentration profiles measured along the depth of the a-GST225 layer in the volume presented in (a).

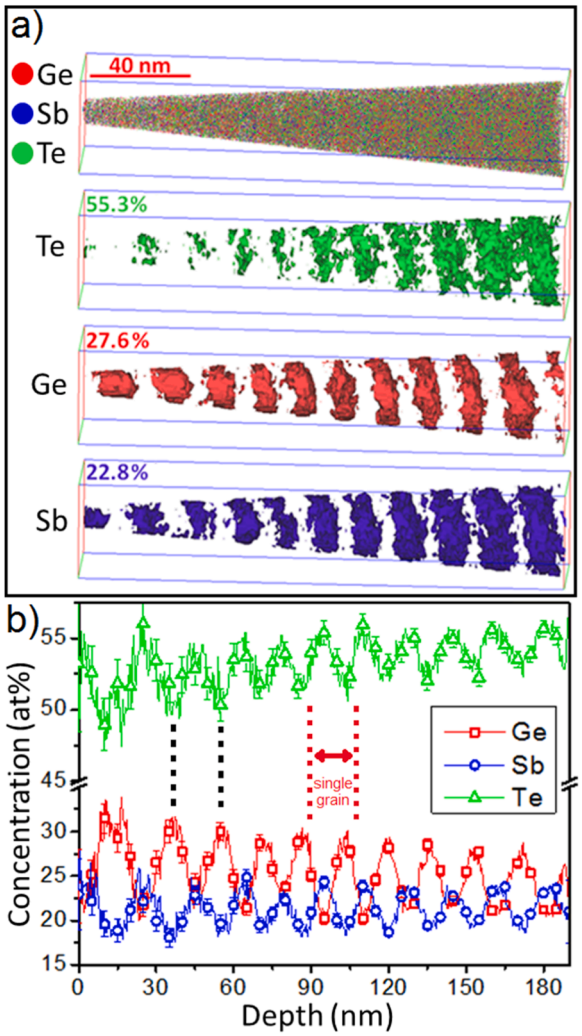

Fig. 4. APT measurements performed on the crystallized GST225 layer: a) same APT volume showing the entire atomic distribution (top volume, each point is a single atom: red for Ge, blue for Sb, and green for Te), as well as Ge, Sb, and Te iso-concentration surfaces delimiting sub-volumes of respective concentrations above 27.6, 22.8, and 55.3 at%; and b) Ge (red squares), Sb (blue circles), and Te (green triangles) concentration profiles measured along the depth of the GST225 layer in the volume presented in (a).

in the film after annealing. The Ge, Sb, and Te concentration profiles measured in the same APT volume (Fig. 4b) confirm the pseudo-periodic distribution of the three elements in the crystallized GST225 layer. 10 (for Ge) to 11 (for Sb and Te) concentration oscillations are observed depending on the element, Sb and Te variations being in phase and Ge variations being in opposition of phase with Sb and Te in the annealed layer. The amplitude (i.e. the concentration difference ΔC) of the oscillations increases towards the GST225 layer surface.

In average, the element concentrations vary in the crystallized layer such as $20 \leq C_{Ge} \leq 30$ at%, $17.5 \leq C_{Sb} \leq 25.0$ at%, and $50 \leq C_{Te} \leq 56$ at %, corresponding to $\Delta C_{Ge} \sim 10$ at%, $\Delta C_{Sb} \sim 7.5$ at%, and $\Delta C_{Te} \sim 6$ at%. These variations are different from that initiated in the amorphous layer, meaning that annealing allowed atoms to diffuse aiming at minimizing the crystal energy. Accordingly, crystallization involved a significant reduction of the average local concentration differences of all the elements: ~ 43% decrease for ΔC_{Ge}, ~ 50% decrease for ΔC_{Sb}, and ~ 70% decrease for ΔC_{Te}. Ge, Sb, and Te composition variations are comprised in the composition ranges initiated in a-GST225, their minimum concentration increased while their maximum concentration decreased during annealing (expected behavior for concentration gradient mediated diffusion). However, Ge variations stayed in opposition of phase with Te variations, while Sb variations are now found to be in phase with that of Te. This behavior may be related to the repulsive tendency of Sb and Ge atoms (phase separation in binary phase diagram) compared to the attractive tendency of Sb and Te atoms (binary compound formation). It is interesting to note that even though Ge and Sb composition variations are observed to vary below and above the 22 at% concentration of the "225" stoichiometry, the Te maximum concentration in the annealed layer corresponds to that of the "225" stoichiometry (i.e. Te concentration variations are limited to occur below 56 at% in the crystallized layer). This difference between Ge and Sb local concentration variations and Te concentration variations may be related to the structure of the GST225 compound. Indeed, Ge and Sb are known to randomly occupy atomic sites belonging to a same sublattice (cation sites) with a significant amount of structural vacancies [43–45], while Te atoms occupy a different sublattice (anion sites). The periodic concentration oscillations in Fig. 4b can be considered to correspond to two different compounds: a Ge-rich compound and a Ge-poor compound, both accepting some stoichiometry variations. According to APT measurements, the stoichiometry exhibiting the highest Ge content corresponds to $Ge_{2.86}Sb_{1.61}Te_{4.46}$, while the stoichiometry exhibiting the lowest Ge content corresponds to $Ge_{1.88}Sb_{2.05}Te_5$, the latter being closer to the "225" stoichiometry.

Fig. 5a presents a STEM high-angle annular dark-field (HAADF) image of the crystallized GST225 layer in cross-section. The contrast observed in this image is mainly due to crystalline disorientation as a long camera length of ~ 195 mm was used for this STEM HAADF image. EDS measurements were performed on the same TEM lamella. An example of the comparison between STEM HAADF and two-dimensional (2D) EDS mapping performed on a same sample region is shown in Fig. 5b (red for Ge and blue for Sb). The GST layer is fully crystallized (no amorphous region) exhibiting a thickness ~ 288 nm. All the grains exhibit the same fcc structure, the contrast differences observed between grains being linked to a difference of lattice orientation. Fig. 5c shows EDS composition profiles measured on the entire thickness of the GST layer. Te exhibits an almost constant composition profile around $C_{Te} \sim$ 51 at%, while Ge and Sb present 15 periodic concentration variations in opposition of phase with $17.5 \leq C_{Ge} \leq 27.5$ at% ($\Delta C_{Ge} \sim 10$ at%) and $22.5 \leq C_{Sb} \leq 30.0$ at% ($\Delta C_{Sb} \sim 7.5$ at%). EDS results agree with APT measurements considering a usual error of 3% in EDS estimations. In particular, one can note that the Te concentration oscillations are not clearly evidenced by EDS, as APT showed that Te variations do not exceed 6 at% that is precisely in the range of EDS measurement uncertainties (± 3%). Furthermore, Sb composition is overestimated while Te composition is underestimated in EDS profiles, due to the overlapping of Sb and Te EDS signals (L transitions in the 3 to 5 keV range), making difficult the separation of Sb from Te (use peak deconvolution).

Nevertheless, one can note that ΔC_{Ge} and ΔC_{Sb} were found to be identical for APT and EDS. 2D EDS element mapping (Fig. 5b) confirmed that the observed composition variations occur in single GST225 grains. In particular, each grain contains in its center the interface between the Sb-rich region (at the bottom of the grain) and the Ge-rich region (on top of the grain). Consequently, the local concentration variations (6 to 10 at %) observed in the annealed sample correspond to stoichiometry variations accepted by the fcc-GST225 phase. STEM (Fig. 5a) shows that two amorphous layers are located on top of the crystalline GST225 layer. According to EDS, the fcc-GST225 layer is in contact with a 7 nm-thick amorphous Ge layer (a-Ge), which is covered by an 8 nm-thick Ge oxide layer, the latter being made of a 5 nm-thick GeO_x layer (with $x > 1$) at the surface of the sample and a 3 nm-thick GeO layer in contact with the amorphous Ge layer. The 10 nm-thick Ge cap prevented oxidation of the GST225 layer, and low annealing temperature prevented the crystallization of the non-oxidized Ge located below the Ge native oxide, allowing fcc-GST225 to nucleate in bulk. However, the fcc-GST225 layer is made of the stack of 15 polycrystalline layers from top to bottom (Fig. 5a), meaning that nucleation was neither homogenous nor random

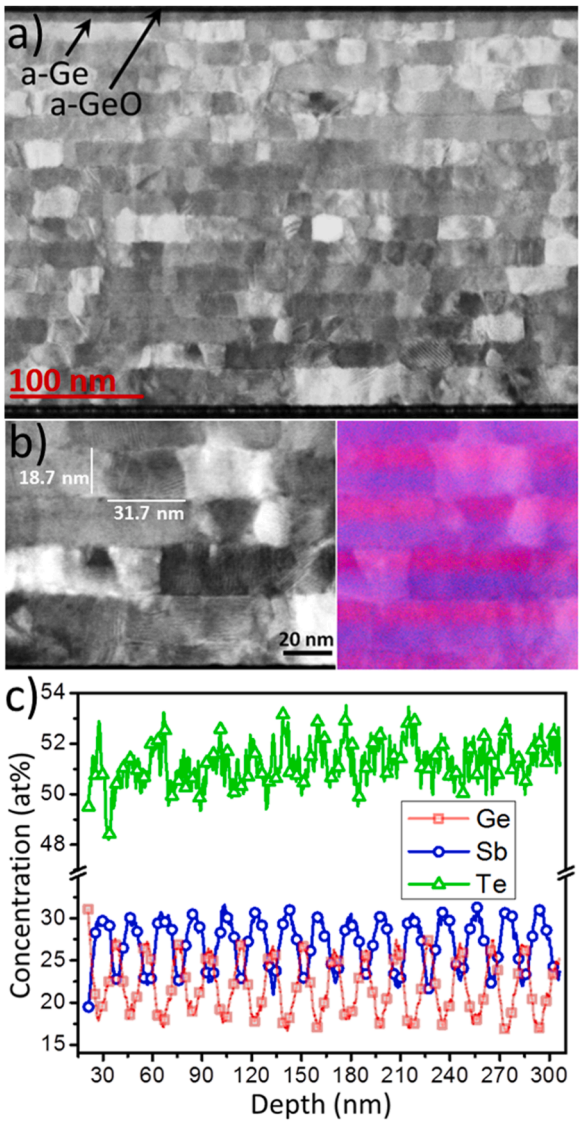

Fig. 5. TEM observations performed on the crystallized GST225 layer in the cross-section geometry: a) STEM HAADF image, b) comparison between the STEM HAADF signal and EDS measurements (red for Ge and blue for Sb) performed on the same region of the sample, and c) Ge (red squares), Sb (blue circles), and Te (green triangles) composition profiles determined by EDS along the depth of the GST225 layer.

in the layer as generally reported for homogeneous a-GST225 layers [46], and the crystallization temperature was found to be 140 °C [26], much lower than generally expected for non-oxidized a-GST225 [16]. The formation of the 15 polycrystalline layers is obviously related to the concentration variations resulting from the 15 rotations of the sample during co-sputtering, and linked to the distribution of fcc-GST225 nuclei in the initial a-GST225 film. Indeed, the grains of the different layers obviously nucleated simultaneously and grew concurrently in the a-GST layer until they were in contact. Fig. 3b shows that Te concentration maximums were located at the same depth as the interface between the Ge-rich and Sb-rich regions in the as-deposited layer. The fact that the $Ge_{2.86}Sb_{1.61}Te_{4.46}/Ge_{1.88}Sb_{2.05}Te_5$ interfaces are incorporated in the grains of each of the 15 layers (Fig. 5b) strongly suggests that the fcc-GST225 phase simultaneously nucleated at each Te concentration maximums distributed along the thickness of the a-GST225 layer, promoting a lower crystallization temperature (heterogeneous nucleation) and leading to the microstructure shown in Fig. 5a.

4. Conclusion

In summary, the crystallization of a 300 nm-thick amorphous GST film exhibiting an overall stoichiometry matching that of GST225 but containing pseudo-periodic Ge, Sb, and Te local composition variations was studied by APT, XRD, and STEM. The crystallized film is polycrystalline and made of a single phase: the fcc-GST225. This phase is not stoichiometric, exhibiting Ge, Sb, and Te concentration variations of ~ 10 at%, ~ 7.5 at%, and ~ 6 at%, respectively. Compared to the (Ge:2, Sb:2,Te:5) stoichiometry, these concentration variations are found to take place around 22 at% ($20 \leq C_{Ge} \leq 30$ at% and $17.5 \leq C_{Sb} \leq 25.0$ at %) for Ge and Sb (cation site sublattice), but to occur below 56 at% for Te (anion site sublattice). Furthermore, the fcc-GST225 stoichiometries respectively displaying the highest and the lowest Ge content were found to be $Ge_{2.86}Sb_{1.61}Te_{4.46}$ and $Ge_{1.88}Sb_{2.05}Te_5$. The microstructure and the element distributions in the polycrystalline fcc-GST225 film suggest that local concentration variations promote fcc-GST225 heterogeneous nucleation in Te-rich regions of the a-GST film, lowering the crystallization temperature.

Data availability

All the necessary data is available in the main text. Any other relevant data are also available upon request.

CRediT authorship contribution statement

Guillaume Roland: Investigation, Validation, Formal analysis, Data curation, Visualization, Writing – original draft. **Alain Portavoce:** Conceptualization, Methodology, Writing – original draft, Writing – review & editing, Supervision, Project administration, Funding acquisition. **Maxime Bertoglio:** Investigation, Methodology. **Marion Descoins:** Investigation, Methodology. **Jacopo Remondina:** Investigation, Validation. **Frédéric Lorut:** Investigation, Methodology, Project administration. **Magali Putero:** Conceptualization, Methodology, Writing – review & editing, Supervision, Project administration, Funding acquisition.

Declaration of Competing Interest

The authors declare that they have no known competing financial interests or personal relationships that could have appeared to influence the work reported in this paper.

Acknowledgements

The authors would like to thank Elisa Petroni (STMicroelectronics) for her critical review of the article. This work was supported by the French National Association of Research and Technology (ANRT Project 2020/0907).

References

[1] W. Zhang, R. Mazzarello, M. Wuttig, E. Ma, Designing crystallization in phase-change materials for universal memory and neuro-inspired computing, Nat. Rev. Mater. 4 (2019) 150–168.
[2] A. Lotnyk, M. Behrens, B. Rauschenbach, Phase change thin films for non-volatile memory applications, Nanoscale Adv. 1 (2019) 3836–3857.
[3] M. Le Gallo, A Sebastian, An overview of phase-change memory device physics, J. Phys. D Appl. Phys. D 53 (2020), 213002.
[4] S. Raoux, F. Xiong, M. Wuttig, E. Pop, Phase change materials and phase change memory, MRS Bull. 39 (2014) 703–710.
[5] M. Wuttig, S. Raoux, The science and technology of phase change materials, Zeitschrift für anorganische und allgemeine Chemie 638 (2012) 2455–2465.
[6] A. Sebastian, et al., Tutorial: Brain-inspired computing using phase-change memory devices, J. Appl. Phys. 124 (2018).
[7] D. Ielmini, S. Ambrogio, Emerging neuromorphic devices, Nanotechnology 31 (2020), 092001.

[8] F. Disegni, et al., Embedded PCM macro for automotive-grade microcontroller in 28nm FD-SOI, in: Proceedings of the Symposium on VLSI Circuits Digest of Technical Papers, 2019.

[9] F. Arnaud, et al., High density embedded PCM cell in 28nm FDSOI technology for automotive micro-controller applications, in: Proceedings of the Technical Digest - International Electron Devices Meeting, IEDM, 2020, https://doi.org/10.1109/IEDM13553.2020.9371934.

[10] P. Cappelletti, et al., Phase change memory for automotive grade embedded NVM applications, J. Phys. D Appl. Phys. (2020), https://doi.org/10.1088/1361-6463/ab71aa.

[11] A. Redaelli, E. Petroni, R. Annunziata, Material and process engineering challenges in Ge-rich GST for embedded PCM, Mater. Sci. Semicond. Process. 137 (2022), 106184.

[12] J. Meena, S. Sze, U. Chand, T.Y. Tseng, Overview of emerging nonvolatile memory technologies, Nanosc. Res. Lett. 9 (2014) 526.

[13] P.S. Dutta, H.L. Bhat, V. Kumar, The physics and technology of gallium antimonide: An emerging optoelectronic material, J. Appl. Phys. 81 (1997) 5821–5870.

[14] P. Lucas, et al., Telluride glasses for far infrared photonic applications, Opt. Mater. Express 3 (2013) 1049.

[15] G. Bruns, et al., Nanosecond switching in GeTe phase change memory cells, Appl. Phys. Lett. 95 (2009), 043108.

[16] P. Noé, C. Vallée, F. Hippert, F. Fillot, J.Y. Raty, Phase-change materials for non-volatile memory devices: from technological challenges to materials science issues, Semicond. Sci. Technol. 33 (2018) 13002.

[17] Y. Chen, et al., RESET current reduction for phase change memory based on standard 0.13-μm CMOS technology, Procedia Eng. 16 (2011) 401–406.

[18] L.W.W. Fang, et al., Phase change random access memory devices with nickel silicide and platinum silicide electrode contacts for integration with CMOS technology, J. Electrochem. Soc. 158 (2011) 232–238.

[19] G.W. Burr, et al., Phase change memory technology, J. Vacuum Sci. Technol. B 28 (2010) 223–262.

[20] S. Yu, P.Y. Chen, Emerging Memory Technologies: Recent Trends and Prospects, IEEE Solid State Circuits Mag. 8 (2016) 43–56.

[21] J. Kellner, et al., Mapping the band structure of GeSbTe phase change alloys around the Fermi level, Commun. Phys. (2018) 1–11, https://doi.org/10.1038/s42005-018-0005-8.

[22] C. Rios, et al., Integrated all-photonic non-volatile multi-level memory, Nat. Photon. 9 (2015) 725.

[23] F. Arnaud, et al., Truly innovative 28nm FDSOI technology for automotive micro-controller applications embedding 16MB phase change memory, in: Proceedings of the Technical Digest - International Electron Devices Meeting, 2019. IEDM 2018-Decem, 18.4.1-18.4.4.

[24] P. Zuliani, et al., Overcoming temperature limitations in phase change memories with optimized Gex Sby Tez, IEEE Trans. Electron Dev. 60 (2013) 4020–4026.

[25] E Petroni, et al., Metrics for Quantification of By-Process Segregation in Ge-Rich GST, Front. Phys. 10 (2022) 1–9.

[26] A. Portavoce, et al., Kinetic Monte Carlo simulations of Ge-Sb-Te thin film crystallization, Nanotechnology 33 (2022), 295601.

[27] M. Agati, M. Vallet, S. Joulié, D. Benoit, A Claverie, Chemical phase segregation during the crystallization of Ge-rich GeSbTe alloys, J. Mater. Chem. C 7 (2019) 8720–8729.

[28] S. Privitera, et al., Crystallization and phase separation in Ge2+xSb2Te5 thin films, J. Appl. Phys. 94 (2003) 4409–4413.

[29] O. Thomas, et al., Crystallization behavior of N -doped Ge-rich GST thin films and nanostructures: an *in-situ* synchrotron X-ray diffraction study, Microelectron. Eng. 244-246 (2021), 111573.

[30] Agati, M., Gay, C., Benoit, D. & Claverie, A. Effects of surface oxidation on the crystallization characteristics of Ge-rich Ge-Sb-Te alloys thin films. *Appl. Surf. Sci.* 518, (2020).

[31] M.A. Luong, et al., On some unique specificities of Ge-Rich GeSbTe phase-change material alloys for nonvolatile embedded-memory applications, Phys. Stat. Solidi Rapid Res. Lett. 15 (2020), 2000471.

[32] M.A. Luong, et al., Impact of nitrogen on the crystallization and microstructure of Ge-Rich GeSbTe alloys, Phys. Stat. Solidi Rapid Res. Lett. 2000443 (2020) 1–6.

[33] M. Agati, F. Renaud, D. Benoit, A. Claverie, In-situ transmission electron microscopy studies of the crystallization of N-doped Ge-rich GeSbTe materials, MRS Commun. 8 (2018) 1145–1152.

[34] I. Ronneberger, W. Zhang, H. Eshet, R. Mazzarello, Crystallization properties of the Ge2Sb2Te5 phase-change compound from advanced simulations, Adv. Funct. Mater. 25 (2015) 6407–6413.

[35] Y. Xu, et al., Materials screening for disorder-controlled chalcogenide crystals for phase-change memory applications, Adv. Mater. 33 (2021) 1–10.

[36] Y. Xu, et al., Unraveling crystallization mechanisms and electronic structure of phase-change materials by large-scale *ab initio* simulations, Adv. Mater. 34 (2022).

[37] K.J. Choi, et al., The effect of antimony-doping on $Ge_2Sb_2Te_5$, a phase change material, Thin Solid Films 516 (2008) 8810–8812.

[38] A. Debunne, et al., Evidence of crystallization-induced segregation in the phase change material Te-Rich GST, J. Electrochem. Soc. 158 (2011) H965.

[39] N. Ciocchini, et al., Modeling resistance instabilities of set and reset states in phase change memory with Ge-rich GeSbTe, IEEE Trans. Electron Dev. 61 (2014) 2136–2144.

[40] A. Portavoce, K. Hoummada, A. Ronda, D. Mangelinck, I. Berbezier, Si/Ge intermixing during Ge Stranski-Krastanov growth, Beilstein J. Nanotechnol. 5 (2014) 2374–2382.

[41] A. Portavoce, et al., Ferromagnetic MnCoGe thin films produced via magnetron sputtering and non-diffusive reaction, Appl. Surf. Sci. 437 (2018) 336–346.

[42] J. Gutwirth, M. Kotrla, T. Halenkovic, V. Nazabal, P. Nemec, Tailoring of multisource deposition conditions towards required chemical composition of thin films, Nanomaterials 12 (2022) 1830.

[43] T. Matsunaga, N. Yamada, Y. Kubota, Structures of stable and metastable Ge2Sb2Te 5, an intermetallic compound in GeTe-Sb_2Te_3 pseudobinary systems, Acta Crystallograph. Sec. B Struct. Sci. 60 (2004) 685–691.

[44] N. Yamada, T. Matsunaga, Structure of laser-crystallized Ge_2Sb_2+xTe_5 sputtered thin films for use in optical memory, J. Appl. Phys. 88 (2000) 7020–7028.

[45] T. Nonaka, G. Ohbayashi, Y. Toriumi, Y. Mori, H. Hashimoto, Crystal structure of GeTe and $Ge_2Sb_2Te_5$ meta-stable phase, Thin Solid Films 370 (2000) 258–261.

[46] Pierre. Noé, et al., Impact of interfaces on scenario of crystallization of phase change materials, Acta Mater. 110 (2016) 142–148.